Machine Learning-Driven Sensitivity Analysis for a 2-Layer Printed Circuit Board Inductive Motor Position Sensor

Qinghua Lin *, Devin Sullivan, Douglas Moore, Donald Tong

Posted Date: 12 December 2025

doi: 10.20944/preprints202512.1156.v1

Keywords: inductive motor position sensor; routing strategy; machine learning; Extreme Gradient Boosting; SHapley Additive exPlanations; Fourier series; accuracy

 doi:10.20944/preprints202512.1156.v1

Article

Machine Learning-Driven Sensitivity Analysis for a 2-Layer Printed Circuit Board Inductive Motor Position Sensor

Qinghua Lin [1,*], Devin Sullivan [2], Doug Moore [1] and Donald Tong [1]

[1] CTS Corporation, 905 W Blvd North, Elkhart, IN 46514, USA

[2] Independent Researcher, USA

* Correspondence: linqh314@gmail.com

Abstract

Motor position sensors are critical parts for traction motors control in electrified automotive powertrain. As motors are getting more compact due to the advance of technology the packaging space for motor position sensors is becoming increasingly restricted. This study presents a two-layer (2L) printed circuit board (PCB) routing strategy for inductive motor position sensors with limited area. A prototype was fabricated and tested on a test bench using a comprehensive design of experiments that contains 625 combinations of X- and Y-offsets, tilt angle, and airgap at various levels (±0.5 mm in X/Y, ±0.5° tilt, 1.9–3.1 mm airgap). Across the tolerance box, the accuracy under all test cases remained within ±1 electrical degree. The accuracy analysis through Fourier series on circle shows that the DC offset and magnitudes mismatch of the 3 Rx signals are the dominant error contributors due to the routing modification. An Extreme Gradient Boosting (XGBoost) model was trained and validated with R^2 = 0.9951 on the sensor data. The SHapley Additive exPlanations (SHAP) analysis identified tilt and Y-offset as dominant contributors to accuracy degradation. The model revealed a mild Y-axis asymmetry introduced by routing modifications. The SHAP results show that machine learning workflow provides a general, quantitative framework for analyzing inductive sensor layouts and installation tolerances.

Keywords: inductive motor position sensor; routing strategy; machine learning; Extreme Gradient Boosting; SHapley Additive exPlanations; Fourier series; accuracy

1. Introduction

The global move toward electrified mobility [1] requires precise control on the performance and reliability of electric motor control systems. Accurate rotor position feedback is essential for maximizing the efficiency and torque output of traction motors [2–4]. Motor position sensors are critical to achieve this task, which must survive the severe operational environment of the motor, including high temperatures, intense vibration, corrosive contaminants, and significant electFromagnetic interference (EMI) [5]. Traditionally, electromechanical resolvers have been the established standard for high-accuracy and robust position sensing in traction motor applications [5–7]. Resolvers are reliable and robust, but they come with drawbacks: their wound-coil stator and rotor structures contribute to significant weight and bulk, complexity in manufacturing, and higher unit cost due to precision winding requirements. While excellent in performance, their form factor and cost implications are increasingly challenging for high-volume, compact EV powertrains. Other encoder technologies, such as optical or magnetic encoders, often face their own limitations in harsh automotive environments, including sensitivity to dirt, condensation, stray magnetic fields, and temperature drift.

Inductive motor position sensors offer an alternative. Utilizing printed circuit board (PCB) based coil structures reduce weight and size, lower manufacturing complexity, and resistance to stray

 doi:10.20944/preprints202512.1156.v1

fields. This makes them ideal for the constrained and demanding environment of modern traction motors [8]. Inductive position sensor devices operate by driving a high-frequency excitation current through one or more transmit (Tx) coils, generating an alternating magnetic field. A conductive target modulates this field through eddy-current induction. The resulting mutual coupling between the Tx coils and a set of receive (Rx) coils varies as a function of the rotor angle. By geometrically encoding the Rx coils (often sin/cos or multiphase patterns), the induced voltages reconstruct the absolute rotor position through arctangent demodulation or resolver-like signal processing [9,10]. In an ideal design, the Tx coil generates a spatially uniform magnetic field, and the Rx coils maintain perfect spatial sensitivity, ensuring high linearity and immunity to misalignment. Any disruption of the underlying coil symmetry directly impacts accuracy [11,12].

For high-precision inductive MPS, a 4-layer (4L) PCB architecture supports symmetric Tx/Rx routing, well-controlled return paths, and minimal disturbance to the ideal magnetic field distribution. However, industry pressure toward cost reduction and miniaturization increasingly motivates the transition to 2-layer (2L) PCBs. In many practical applications the Tx coil must span both layers to satisfy dimensional requirements. As a result, routing all Tx and Rx terminals back to the integrated circuit (IC) becomes challenging. These geometric modifications break the magnetic symmetry guaranteed by a 4L stack-up and inevitably introduce excitation-field distortion, which manifests as increased non-linearity in the accuracy. Therefore, the core engineering question is how to achieve a minimally distorted coil topology. In addition, to validate the robustness of such asymmetric designs is challenging due to the interaction of the geometric distortion introduced by routing and mechanical installation tolerances. It is difficult to quantify using traditional sensitivity analyses. To address this, we used Extreme Gradient Boosting (XGBoost)—which is powerful in modeling complicate interactions within high-dimensional datasets [13]. By integrating the XGBoost model with SHapley Additive exPlanations (SHAP) [14,15], we gain insight into the underlying relationships between installation tolerances and sensor accuracy.

This paper presents a 2L PCB inductive motor position sensor (MPS) design that maintains effective Tx/Rx symmetry under strict area constraints. A prototype was built and experimentally evaluated over a 625-point misalignment and airgap tolerance box, demonstrating that the 2L layout achieves ±1 electrical degree despite unavoidable routing modification. In addition, a machine-learning workflow using XGBoost and SHAP was applied to interpret sensitivity to installation tolerances, offering a practical method for robustness analysis and tolerance setting in future inductive MPS designs.

2. Materials and Methods

2.1. 2L-PCB Inductive MPS Design

Inductive MPSs generally have either a full-circle or partial-circle shape. Full-circle designs, as shown in Figure 1a, allow a circular Tx coils to generate a uniform magnetic field along the Rx coils shown in Figure 2. These configurations have strong signal strength and high robustness against installation variations. Partial-circle designs, illustrated in Figure 1b, implement only a portion of the full circle. The partial-circle design enables compact layout and low cost but disrupts field symmetry and very susceptibility to misalignment and mechanical tolerances. The present work focuses on full-circle configurations.

There are mainly three cases regarding PCB layers and arrangement of Tx/Rx coils when balancing performance, manufacturability, and cost (here we are not considering any shielding layers). The selection between a four-layer and two-layer configuration depends primarily on available area for coils layout, Rx coils signal strength, and the degree of routing distortion that can be tolerated without compromising signal integrity.

Case 1--Four-layer (4L) PCB: in space-constrained applications, the 4L configuration provides two main advantages: 1) it preserves Tx/Rx magnetic-field symmetry to maintain strong, balanced

 doi:10.20944/preprints202512.1156.v1

Rx signals, and 2) it offers the routing flexibility needed to connect the coils to the IC. These benefits make the 4L option a robust choice when PCB area is limited.

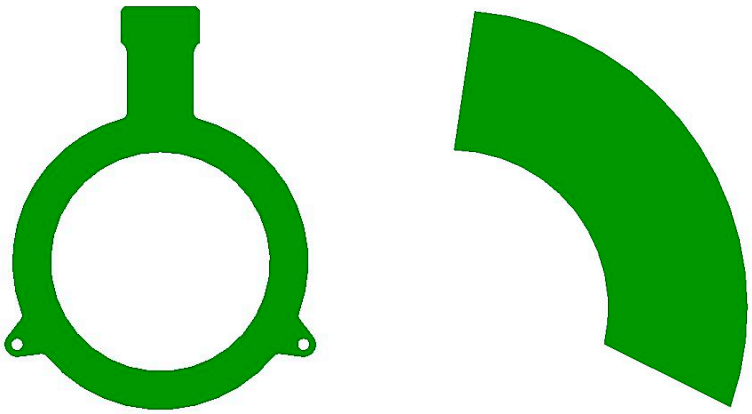

(**a**) (**b**)

Figure 1. Inductive MPSs configurations: (**a**) full-circle configuration; (**b**) partial-circle configuration.

Case 2--Two-layer (2L) PCB with sufficient area: when adequate PCB area is available, the Tx coils can be routed entirely on a single layer. This allows Tx and Rx traces to connect to the IC without modification. This layout provides excellent field balance and accuracy, while the most cost-efficient configuration.

Case 3--Two-layer (2L) PCB with limited area: in this application where PCB area is restricted but diameter is bigger than case 1, a 2L configuration often becomes unavoidable for cost reason. If the Tx occupies a single layer like previous case, the remaining area for Rx routing may be insufficient to induce a strong voltage in Rx. As a result, the Tx and Rx coils need to be layout in both layers. This will introduce asymmetries that increase non-linearity due to the modification of coils routing shown in Figure 2. This configuration, though challenging, represents a realistic case for mass-produced automotive sensors and forms the focus of this study.

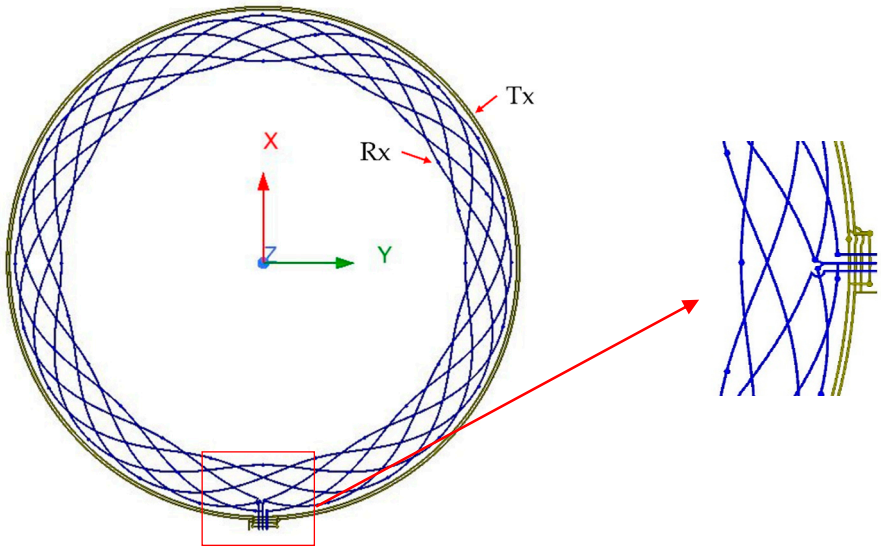

(a) (b)

Figure 2. 2L configuration (a) Layout of the Tx/Rx coils; (b) Zoom-in Tx/Rx routing to the IC.

Figure 2a shows the full layout of the concentric Tx/Rx coils, while Figure 2b zooms in the routing region. The zoomed view highlights the unavoidable geometric asymmetry induced when directing the Tx and Rx traces toward the interface IC. This modification is the primary source of the

 doi:10.20944/preprints202512.1156.v1

magnetic field imbalance in compact 2L designs. The objective of this work is to experimentally evaluate the impact of this routing modification and demonstrate that, despite being unavoidable in compact 2L architectures, the sensor can still achieve the required accuracy and robustness.

The two-layer prototype, shown in Figure 3, evaluated in this work has an outer diameter of 73.2 mm and an inner diameter of 54.5 mm. The Tx coils consist of four turns with two turns on each layer. Both Tx and Rx coils use a trace width of 0.15 mm and 35-μm copper thickness. The excitation frequency was designed at about 3.5 MHz.

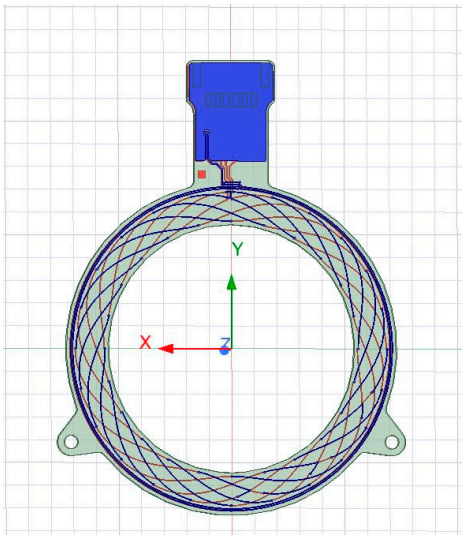

Figure 3. Proposed 2L PCB coil layout and global X–Y coordinate definition.

2.2. Design of Experiments

A structured experimental design was implemented to quantify how mechanical installation or life-long deviations affect the accuracy and robustness of the two-layer (2L) inductive MPS. The mechanical factors—airgap, misalignment along the X and Y axes, and tilt angle—were considered within realistic application limits. Figure 4 illustrates the definition of each installation variable: (a) the airgap between the sensor PCB and the rotating target, (b) X and Y offset, and (c) the tilt angle (θ) representing tilted PCB compared to target along the Y-axis. The nominal condition is defined at x = 0mm, y = 0mm, airgap=2.5mm, and θ = 0°.

Our inhouse test of inductive MPS confirmed that accuracy is independent of rotational speed. Thus, all tests were conducted at a fixed speed of 2000 RPM in this study. In addition, this speed lies near the mid-range of our onsite servo drive capability (maximum 5000 rpm) and was chosen to ensure a consistent condition for all tests. Each factor was evaluated at five levels spanning the normal mechanical tolerance range. The resulting full-factorial matrix, summarized in Table 1, covered 625 combinations of airgap, X/Y offset, and tilt. This factorial structure enables quantification of both single-factor and interaction effects while keeping the total test count within manageable limits.

Table 1. DOE summary.

Factor	Levels	Motor Speed (RPM)
Airgap (mm)	[1.9, 2.2, 2.5, 2.8, 3.1]	2000
X--offset (mm)	[-0.5, -0.3, 0, 0.3, 0.5]	2000
Y--offset (mm)	[-0.5, -0.3, 0, 0.3, 0.5]	2000
Tilt θ (deg)	[-0.5, -0.3, 0, 0.3, 0.5]	2000

 doi:10.20944/preprints202512.1156.v1

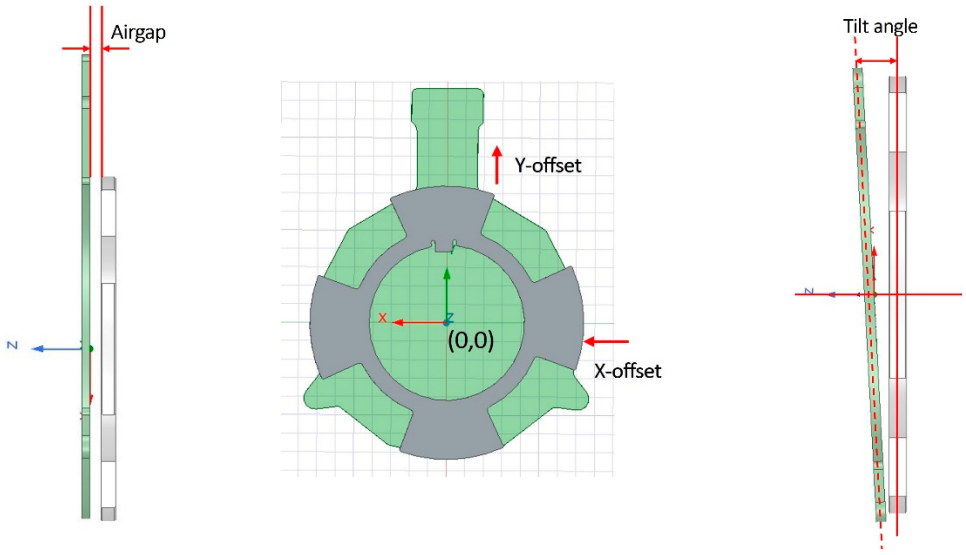

Figure 4. Installation definition: (a) airgap between PCB and the target; (b) X, Y offsets and the origin; (c) tilt angle along Y direction.

For each condition, data recording began after the motor speed reached the target and stable. During each test, the sensor's sine and cosine differential signals were captured simultaneously with the encoder reference angle.

2.3. Experimental Setup

The experimental setup is illustrated in Figure 5. The system was capable to precisely impose and measure geometric misalignments—including airgap, lateral offsets, and tilt angle—while recording synchronized sensor and reference signals. The test cart [Figure 5a] includes the test fixture, PC monitor, and data acquisition and motor control system. The test fixture [Figure 5b] allowed the sensor to be mounted coaxially with the rotating metallic target. The target was driven by a servo motor. The airgap between the sensor and target was adjustable by means of a micrometer-controlled Z-axis stage. Lateral X and Y offsets were introduced using precision translation stages with 0.001 mm resolution, while angular tilt was applied through a rotary stage with accuracy of 0.01° [Figure 5c,d].

Sensor signals were recorded using a National Instruments PCIe-6361 card with simultaneous analog sampling at 25KHz per channel. The reference mechanical angle was obtained from a high-resolution optical encoder (18-bit) mounted on the same shaft. Both sensor and encoder signals were captured synchronously using a shared hardware trigger. Before the experiments, analog channel-to-channel phase skew in the DAQ system was characterized by applying the same input signal to all recording channels. The resulting time offset was measured and compensated in data collection system to ensure precise alignment between the sine and cosine channels. Accurate channel synchronization is particularly critical for high-speed motor applications, where even sub-microsecond skew can introduce a significant phase shift between sine and cosine waveforms, distorting the calculated electrical angle and leading to incorrect evaluation of sensor performance [3,18,19]. All measurements were performed at room temperature (23 ± 2 °C). For each test condition 5 seconds length of data was captured.

 doi:10.20944/preprints202512.1156.v1

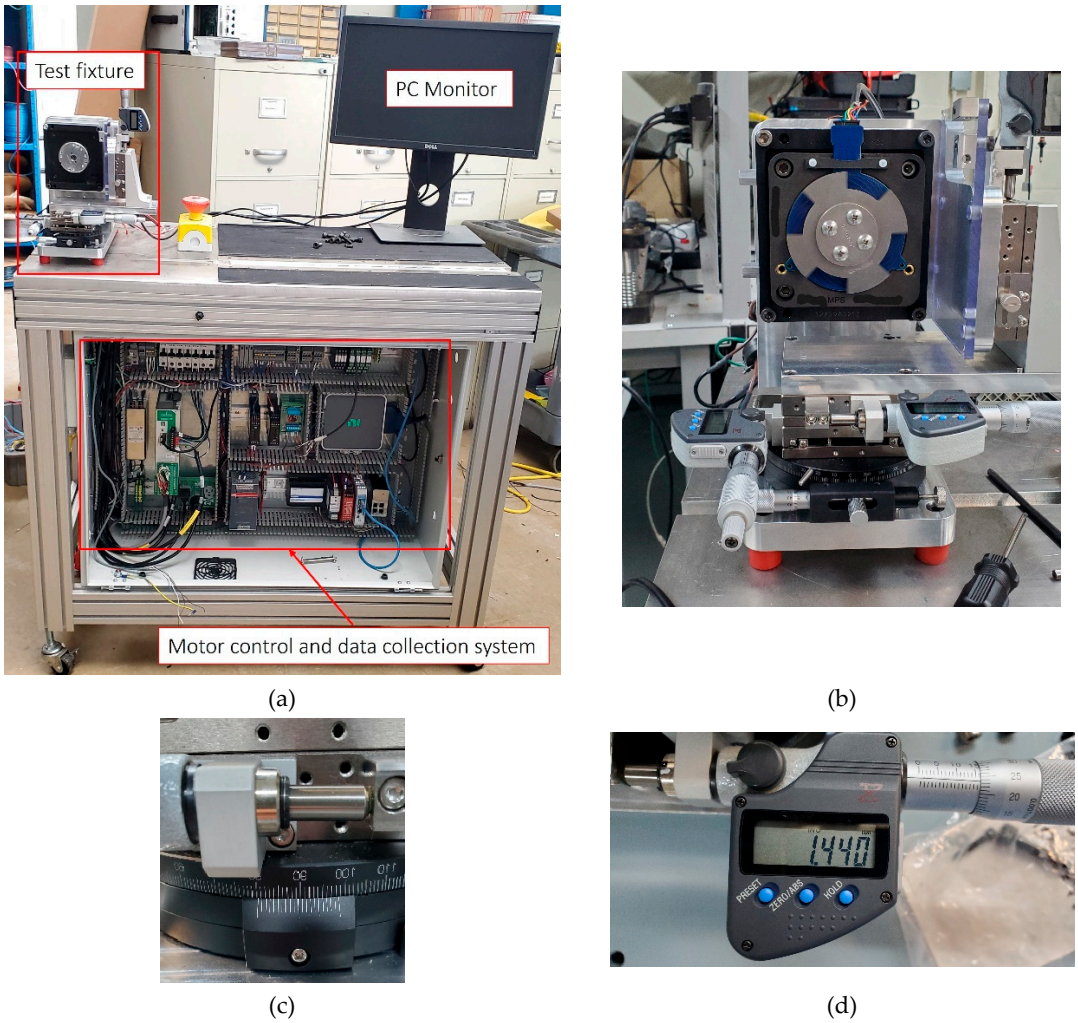

Figure 5. Experimental setup: (a) whole test cart; (b) fixture for sensor attachment and motor; (c) rotary stage for tilt adjustment; (d) x, y, and z misalignment adjustment stages.

2.4. Methods

2.4.1. Definition of Sensor Accuracy and Target Variable

The accuracy of the sensor was quantified as the deviation between the electrical angle calculated from the MPS signals and the reference electrical angle obtained from the encoder, as expressed in Equation (1).

$$\Delta\theta_i = \theta_{mps,i} - \theta_{ref,i} \quad (1)$$

The MPS electrical angle was computed from the sine and cosine signals:

$$\theta_{mps,i} = atan(\frac{sin_i}{cos_i}) \quad (2)$$

The reference electrical angle was derived from the encoder's mechanical angle according to:

$$\theta_{ref,i} = mod(\varphi_i \times N + \theta_{offset}, 360) \quad (3)$$

where $\theta_{mps,i}$ represents calculated electrical angle from inductive MPS, which is calculated by Equation (2); $\theta_{ref,i}$ is the reference electrical angle converted from encoder angle which is a mechanical angle. The relationship between electrical angle and mechanical angle can be expressed in Equation (3), where φ_i represents the encoder reading; N is the number of pole pairs of the motor; θ_{offset} is a fixed electrical-angle offset determined under nominal mechanical alignment. The sin_i

 doi:10.20944/preprints202512.1156.v1

and cos_i are the inductive MPS voltage outputs. For each sensor prototype, the offset was first determined under the nominal alignment condition and subsequently held during accuracy evaluations at all conditions.

The voltage from Rx coils (U, V, and W) can be expressed as Equation (4). $A_{u,i}$, $A_{v,i}$, and $A_{w,i}$ are the harmonic coefficients of the 3 Rx signals, representing the signal magnitudes. Ideally, all the even harmonics are rejected by the clockwise and counterclockwise turning loops design in the coils, while odd terms are left in the system [9]. c_u, c_v, and c_w are the DC offsets. These DC offsets are caused by imbalance between the clockwise and counterclockwise winding in the Rx coils [11]. In a perfect design and manufacturing process, we expect U, V, and W have identical harmonic coefficients without any DC offset because any difference among the harmonic coefficients and existence of DC offset will all turn into angle errors.

$$\begin{cases} U = \sum_{i=1}^{\infty} A_{u,i} cos(i\theta) + c_u \\ V = \sum_{i=1}^{\infty} A_{v,i} cos\left(i\theta - i\frac{2\pi}{3}\right) + c_v \\ W = \sum_{i=1}^{\infty} A_{w,i} cos\left(i\theta + i\frac{2\pi}{3}\right) + c_w \end{cases} \quad (4)$$

Since the angle error $\Delta\theta$ is a periodic function of the electrical angle it can be approximated by a Fourier series on the circle, as Equation (5). A_n is the amplitude and φ_n is the phase of nth order harmonic. According to references [11] and [9], DC offsets in U, V, and W will show up in the angle error as first order harmonic; mismatch of Rx signals amplitudes will express as 2nd order harmonic in the error; other higher order harmonic in the U, V, and W will enter the angle error as higher order (>2 order) harmonic. By decomposing angle errors in Fourier fashion, we can identity the underlying design non-idealities.

$$\Delta\theta = \sum_{n=1}^{n} A_n cos(n\theta + \varphi_n) + a_0 \quad (5)$$

In the machine learning regression model, a target variable (y) is constructed as the model output expressed in Equation (6). For each mechanical condition, instead of directly using the sensor average error as the target, we normalized errors by comparing to the nominal condition average error and scaled by 100. Multiplying by 100 converts the normalized deviation into bigger level, which improves numerical stability during model training and ensures that small variations in accuracy are adequately represented by the regression algorithm [16].

$$y = \left[\frac{\sum_1^n(|(\theta_{mps,i} - \theta_{ref,i}|)}{n} - \left(\frac{\sum_1^n(|(\theta_{mps,i} - \theta_{ref,i}|)}{n}\right)_{nominal}\right] \times 100 \quad (6)$$

Figure 6 displays the distribution of all target variables. The boxplot highlights the spread of installation-induced accuracy deviations. This skewed distribution indicates that certain installation perturbations induce larger angle deviations than others. Characterizing the target variables in these areas provides insight for specific installation conditions that lead to elevated accuracy degradation.

2.4.2. Extreme Gradient Boosting (XGBoost)

XGBoost is an ensemble learning technique based on gradient boosting decision trees, originally proposed by Chen and Guestrin [13]. It constructs an additive series of weak learners—typically shallow trees—where each subsequent tree is trained to correct the residual errors of the previous ensemble [17]. This sequential approach allows XGBoost to reduce both bias and variance, achieving strong generalization even with highly nonlinear feature interactions. Its robustness, scalability, and high predictive performance on tabular datasets make it a great fit to model the nonlinear relationship between mechanical installation tolerance and accuracy.

 doi:10.20944/preprints202512.1156.v1

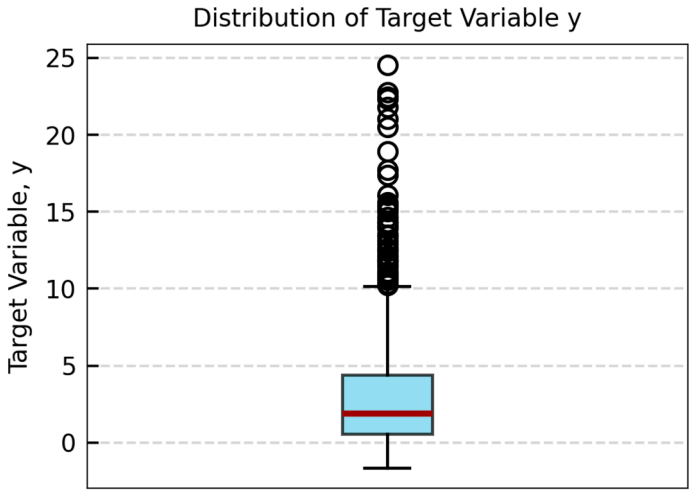

Figure 6. Target values for all the data, including training and validating datasets.

In this study, we implement the XGBRegressor from the xgboost 3.0.5 library in Python. Input features include X- and Y-offsets, airgap, and tilt angle. The model was trained with 70% of the dataset (437 cases) and validated on the remaining 30% (188 cases). To ensure robustness, a 5-fold cross-validation was conducted on the training set within the Optuna Bayesian optimization framework. The optimized hyperparameters included the number of estimators, learning rate, maximum tree depth, minimum child weight, subsampling ratio, column sampling ratio, L1 and L2 regularization terms, and the minimum loss reduction parameter. The model training process followed three stages:

1. Cross-validation optimization: For each Optuna trial, a 5-fold cross-validation was performed to compute the mean RMSE, which served as the objective metric to minimize.
2. Model selection and retraining: After 6000 trials, the best hyperparameters were identified and used to retrain the final model on the full training dataset.
3. Final evaluation: The optimized model was then applied to the independent 30% test dataset to generate predicted accuracy values.

The performance of XGBoost model was assessed using the coefficient of determination (R^2), root mean square error (RMSE) and mean absolute error (MAE) on the test dataset. A scatter plot of predicted versus measured accuracy values was also produced to visualize agreement between model predictions and true values, as shown in Figure 10.

2.4.3. SHAP

To interpret the internal decision process of the XGBoost model and quantify the contribution of each geometric variable to the predicted sensor accuracy, the SHAP framework was used. SHAP provides a unified, theoretically grounded approach for assigning feature importance in complex machine-learning models [14,15]. In the SHAP framework, each feature is treated as a "player" in the model, and its SHAP value ($\emptyset_j$) represents the contribution of that feature to the model output. For a given sample, the prediction from the XGBoost model can be expressed as the sum of the baseline value (the mean value of the target variables) and the additive contributions of each feature, as shown in Equation (7):

$$y = \emptyset_0 + \sum_{j=1}^{M} \emptyset_j x_j \quad (7)$$

where $\emptyset_0$ is the base value, which is the average model output across the entire training dataset. M is the number of input features, which in our case is 4. x_j is a binary input (where $x_j = 1$ if feature j

 doi:10.20944/preprints202512.1156.v1

is present, and $x_j = 0$ if it is absent). The SHAP values were computed using the TreeExplainer algorithm implemented in the *SHAP 0.48.0* Python package. In this paper, we choose to visualize of the SHAP results by using Beeswarm plots and dependence plots [20].

3. Results and Discussion

3.1. Accuracy and Robustness over the Tolerance Box

The result in Figure 7 displays the calculated electrical angle against the mechanical angle under nominal mechanical condition. The angle signal repeats four times across the 360° mechanical range, confirming the prototype is correctly configured for a motor with 4 pole-pairs (P=4). From the figure we can also see that there is an angle offset between the encoder and the MPS angle zeros.

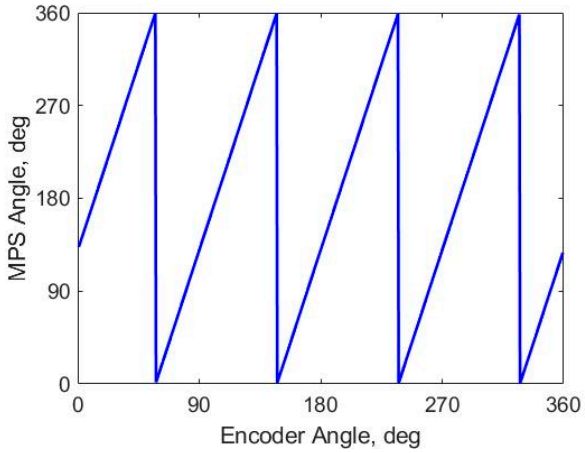

Figure 7. Calculated electrical angle from MPS vs reference encoder.

The corresponding electrical angle error is displayed in Figure 8a. The errors look like a cosine/sine waveform. It has two upper peaks and two lower peaks. However, the lower and upper peaks have different amplitudes. The results show that the error is dominated by 1st and 2nd order harmonics. In Figure 8a, the mean error is also included. The mean error was calculated by dividing the 360° into 180 bins (2° per bin) and averaging all samples within the bin. The selection of number of bins took into consideration of the data sampling rate (25KHz) and motor speed (2000RPM). This ensured that at each bin there were enough data for analysis. From the figure we can see the errors exhibit a relatively wide band, indicating substantial cycle-to-cycle variation. This phenomenon is mainly caused by lobe-to-lobe variation of the target (lobe shape, surface texture, and other manufacturing non-uniformities) and misalignment of the sensor and target.

The mean angle errors were used to do Fourier decomposition to obtain the Fourier coefficients, A_n, φ_n and a_0 in Equation (5). The result is summarized in Table 2. a_0 is the DC term which is mainly determined by the θ_{offset} and carries little information about the design non-idealities. We removed the DC component before we conducted Fourier decomposition. That is why the a_0 in the table is so small and negligible. From the amplitude results listed in Table 2 it is evident that the 1st and 2nd order harmonics dominant the spectrum, while higher orders are much smaller. In these two dominant harmonics, the magnitude of 2nd order is double of the 1st order. The 2nd order electrical harmonic error, which would arise from uncompensated amplitude mismatch. This implies that our routing strategy does affect the balance of the symmetric Rx coil. However, its impact is the about 0.135° which is well acceptable. The appearance of the 1st order electrical harmonic confirms that the DC offsets in Equation (4) are sensitive to air-gap variation. Because the offset calibration was performed at an airgap of 3.1 mm--recommended by the IC supplier and validated in-house as the optimal calibration condition.

 doi:10.20944/preprints202512.1156.v1

Table 2. Harmonic coefficients.

Order	Amplitude A_n (deg)	Phase φ_n (rad)
0 (a_0)	6.5534e-18	0
1	0.0686	-0.5592
2	0.1350	1.8352
3	0.0234	2.2289
4	0.0200	-0.9133
5	0.0032	-0.4544
6	0.0158	-1.3024
7	0.0025	1.5137
8	0.0020	-0.1020
9	0.0014	-0.5425
10	8.7534e-04	-3.0656

Figure 8b shows the comparison of the mean error over electrical cycle and reconstructed error curves based on first two harmonics and first three harmonics. The good overlap between the mean error and assembled curve by first two order harmonics confirms that the error is largely governed by the first 2 order harmonics. Including 3rd harmonic improves approximation on the peaks but does not change the overall curve shape. This indicates the deviation from ideal 120° electrical phase spacing in three-coil layout and lobe-to-lobe variation of the target are present but very small.

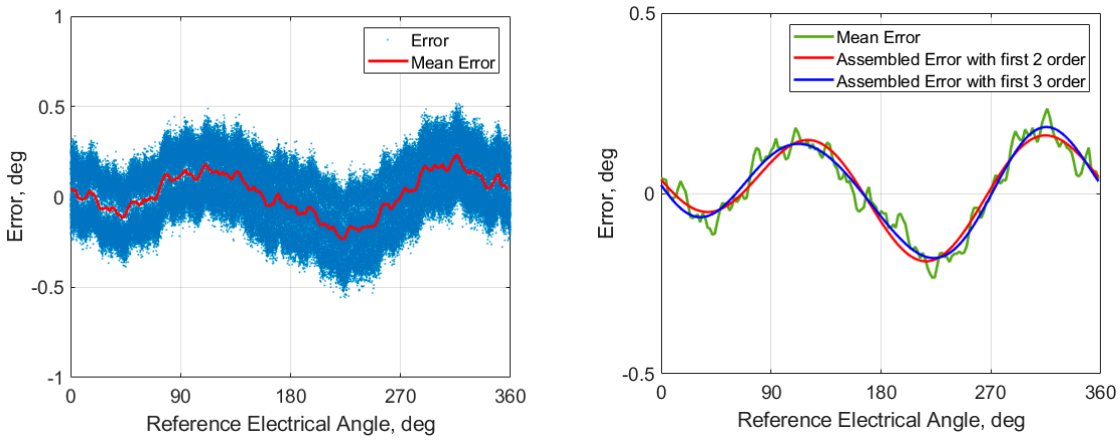

(a) (b)

Figure 8. Under nominal mechanical condition (a) MPS angle errors and mean errors; (b) Comparison of mean error and assembled error by using first two and three orders obtained from FFT analysis.

Figure 9 summarizes the maximum and minimum electrical angle errors across all 625 tested conditions. The Test Case # axis follows the systematic sweep of the full-factorial experimental design with tilt angle changing sequentially from -0.5° to 0.5°. The narrow vertical spread between the maximum and minimum values reveals that angle error remains well-bounded under mechanical perturbations. The fact that no data point exceeds the ±1 electrical-degree limit confirms the robustness of the two-layer design even in the worst-case combinations of misalignment and tilt. A pattern can be observed that increasing tilt angle generally produces a larger deviation in the measured angle (as the test case # increases, tilt angle changes from -0.5° to 0.5°). This is consistent with the expectation that tilt of the PCB or target perturbs the effective coupling area more strongly than lateral offset. Overall, the results presented in Figures 8 and 9 demonstrate that the proposed limited area 2L PCB can achieve ±1 electrical-degree accuracy under all tested conditions and validated that the routing modifications does not compromise robustness.

 doi:10.20944/preprints202512.1156.v1

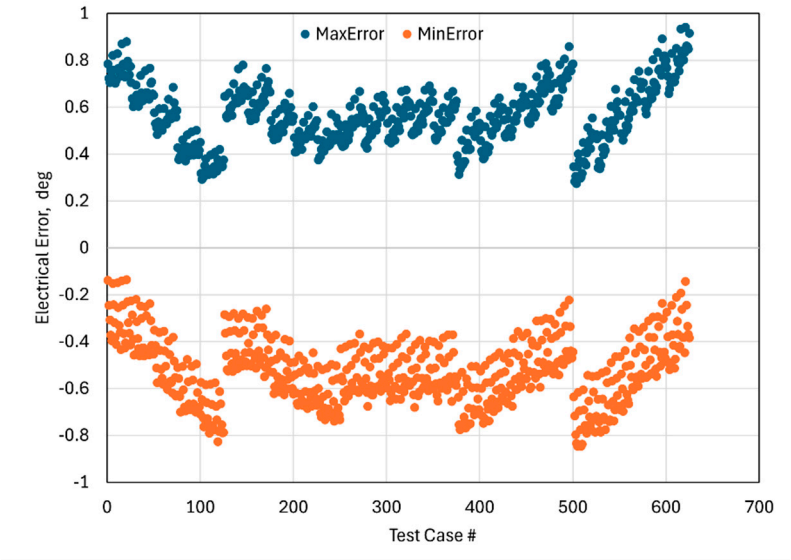

Figure 9. Maximum and minimum electrical angles for 625 test cases.

3.2. XGBoost and SHAP

The comparison of the predictions of the final XGBoost model on the independent 30% test dataset and ground truth is shown in Figure 10. This result demonstrated XGBoost's excellent predictive accuracy in capturing the nonlinear relationships between installation geometry and sensor accuracy degradation. The coefficient of determination (R^2) is 0.9951. The Root Mean Squared Error (RMSE) is 0.3105, which represents the standard deviation of the residuals in the original units of the target variable. The Mean Absolute Error (MAE) is 0.2192, indicating the average prediction deviation is less than a quarter of a unit. These statistics demonstrate that the XGBoost model is highly robust and reliable for accurate predicting installation-induced accuracy degradation.

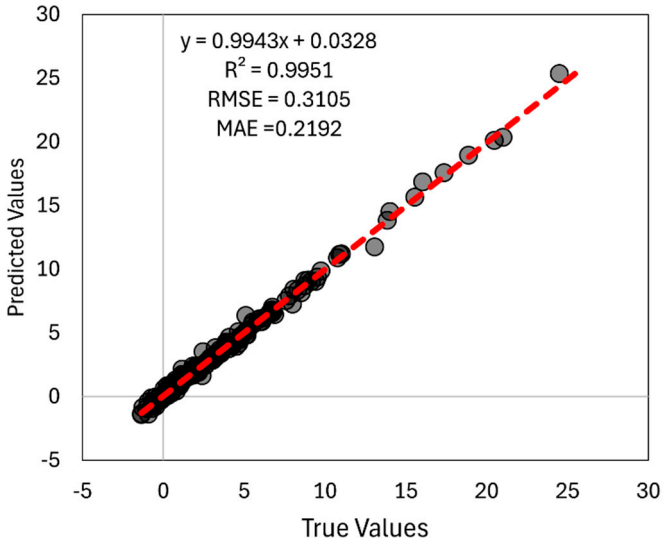

Figure 10. True values vs Predicted values.

Figure 11 presents the SHAP summary (beeswarm) plot for the trained XGBoost model. Each point corresponds to one sample, with color representing the actual feature value (blue = low, red = high) and the horizontal axis showing its SHAP impact on the predicted values. Tilt angle displays the broadest spread (−4 to +8), confirming its dominant influence on sensor accuracy. The larger tilt angle leads to larger SHAP value, which as we can see from the figure that SHAP values bigger than

 doi:10.20944/preprints202512.1156.v1

4 were colored red and blue. Y-offset shows the second-largest dispersion in SHAP values approximately -3.5 to +6.5. Similar to tilt, larger magnitude of Y-offsets, regardless of sign, lead to larger SHAP values, as shown in the figure, generally worsen accuracy. Interestingly, small Y-offsets (purple points) are associated with negative SHAP values. This behavior indicates that the modified Tx/Rx routing (shown in Figure 3) makes the system sensitive to very small Y-offsets. X-offset produces a narrower, near-symmetric SHAP distribution (-3 to +3) centered around zero. Large positive X-offsets (red points) produce positive SHAP values, while large negative X-offsets (blue points) produce negative SHAP values, and small X-offsets cluster near SHAP ≈ 0. This indicates that the Tx/Rx geometry remains symmetric in the X-direction. Airgap exhibits the small overall SHAP magnitude (-2 to +4.5), indicating a weaker contribution compared with the other factors. The lowest airgap value (blue points) tends to have positive SHAP values. In theory, a smaller airgap increases the induced voltage in the Rx coils and thus the DC offset, which as a result leads to the predicted accuracy degradation.

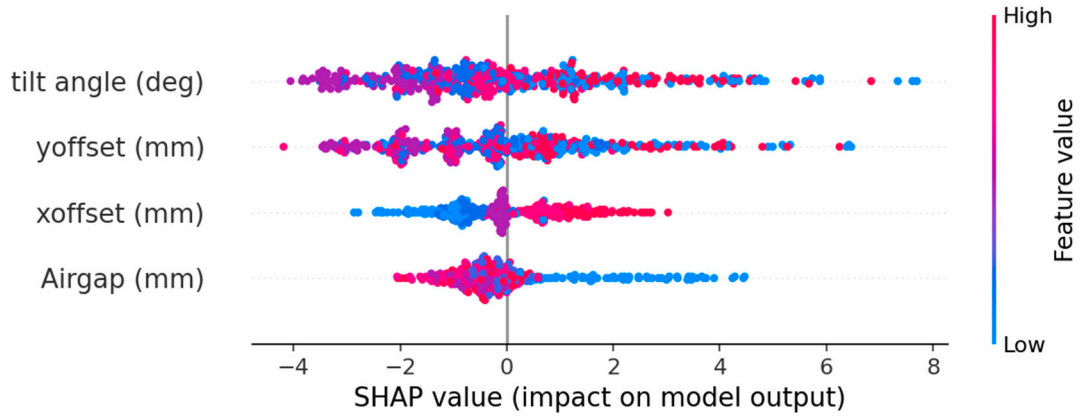

Figure 11. Beeswarm plot of SHAP value reveals the features effects on the model outputs.

The SHAP dependence plots in Figure 12 reveal how feature interactions shape performance and provide physical insight into coupled geometric sensitivities. In Figure 12a, it shows SHAP dependence of airgap with points colored by tilt angle. For small airgaps (1.9, 2.2, and 2.5 mm), the points at each level display a mixed color pattern, indicating that the SHAP contribution of airgap is largely independent of tilt and no dominant tilt effect is expressed. At the largest airgap (2.8 and 3.1 mm), however, a color separation appears: positive tilt angles (red points) are associated with higher SHAP values and negative tilts (blue points) with lower SHAP values, revealing a stronger airgap–tilt interaction in this region. Figure 12b and Figure 12c show SHAP dependence of airgap with points colored by X-offset and Y-offset, respectively. They show similar effect as Figure 12a. However, the red and blue samples in both plots remain largely intermingled at each airgap level, with no consistent vertical gradient, indicating that neither X-offset nor Y-offset influenced the specific airgap impact on sensor accuracy. Figure 12d and Figure 12e show the SHAP dependence of the X-offset feature with points colored by tilt angle and Y-offset, respectively. The X-offset dependence plot in Figure 12d shows that the sign of the SHAP contribution is mainly set by the sign of X-offset (negative offsets yield negative SHAP, positive offsets yield positive SHAP), whereas tilt angle acts as an interacting factor that changes the magnitude of this contribution rather than systematically reversing its sign. Negative Y-offset tends to pull the SHAP contribution of X-offset toward zero, while large positive Y-offset pushes it further away from zero in the direction of the X-offset sign, thereby amplifying the impact of X-misalignment on accuracy. Combined with the global SHAP ranking (Figure 11), this suggests that X-offset has a relatively small, nearly symmetric influence on the predicted target values. Its interactions with tilt and Y-offset are secondary compared with the dominant main effects of tilt and Y-offset themselves. Figure 12f shows the SHAP dependence of Y-offset with points colored by tilt angle. At Y-offset = 0 mm, SHAP values spread a narrow range, indicating small contribution from tilt when the target is centered. As Y-offset moves away from 0mm

 doi:10.20944/preprints202512.1156.v1

the SHAP values rise sharply, especially at +0.5 and -0.5 mm where many samples exceed +4 units, indicating that Y-offset is one of the drivers of increased target values. The color distribution indicates a pronounced interaction with tilt: positive Y-offset and positive tilt reinforce each other and jointly amplify the Y-offset contribution to error, while opposite-signed tilts partially compensate it. The result demonstrates that Y-direction misalignment—especially when combined with tilt—is one of the dominant sources of installation-induced accuracy degradation and captures the directional sensitivity introduced by the Y-aligned Tx/Rx routing modification.

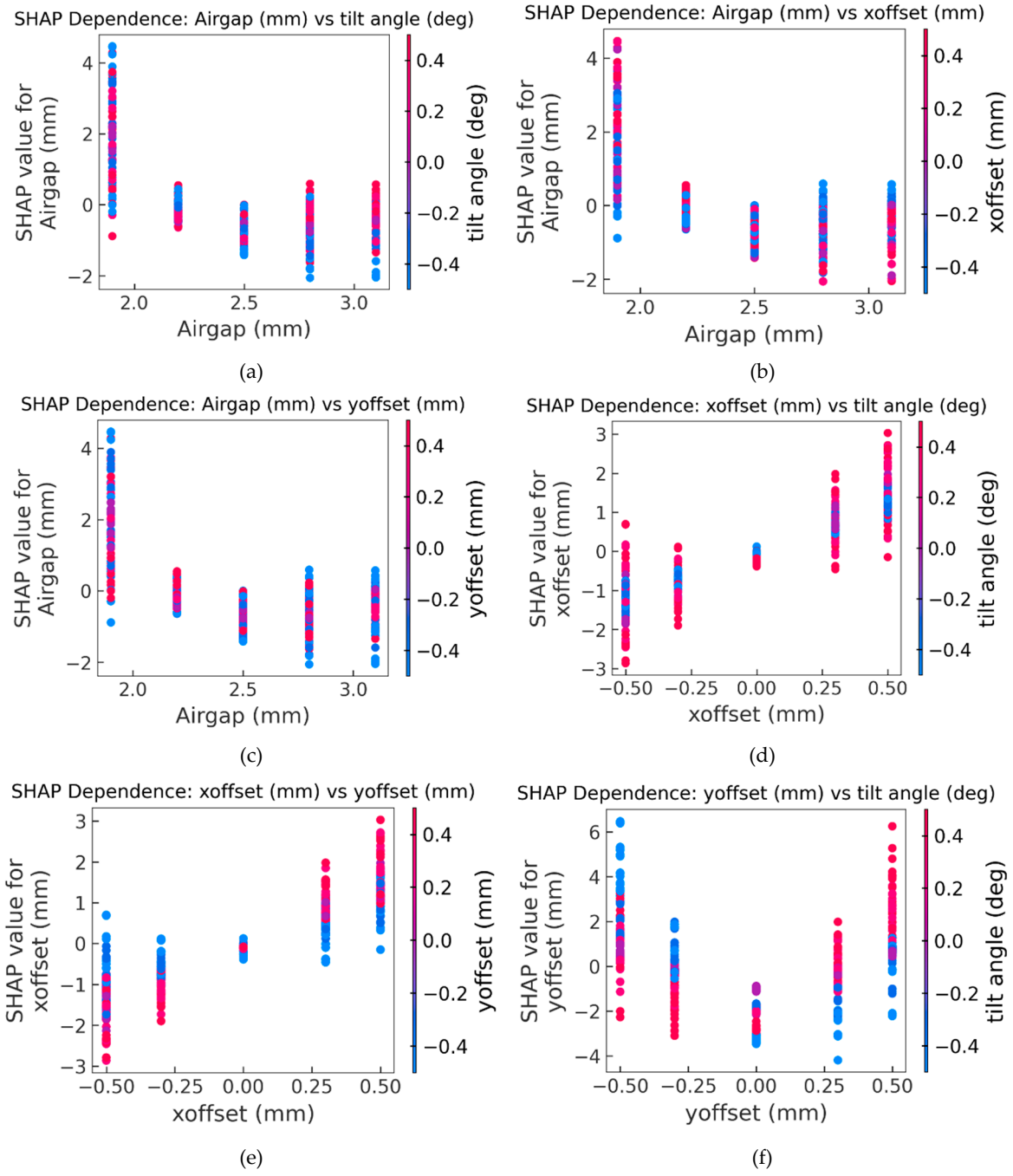

Figure 12. Dependence plots (a) airgap interacts with tilt; (b) airgap interact with x offset; (c) airgap interacts with y offset; (d) x offset interacts with tilt; (e) x offset interacts with y offset; (f) y offset interacts with tilt.

3.3. Practical Guidance for Design and Tolerance Specification

The present work demonstrates a general workflow that can be used to analyze inductive MPS layouts and quantify installation tolerances impact on sensor accuracy. The procedure consists of: (1)

 doi:10.20944/preprints202512.1156.v1

Measuring sensor accuracy under a realistic mechanical tolerance box in terms of X/Y offsets, tilt, and airgap; (2) decomposing angle error into harmonics to identify dominant components and link them to specific design features; (3) training a regression model (here, XGBoost) as a fast surrogate of the sensor response; and (4) applying SHAP analysis to rank misalignment dimensions and resolve their main effects and interactions.

In practice, the harmonic decomposition directly links to specific layout features and thus, it can help to optimize the sensor designs. For example, if the Fourier analysis shows larger 2nd order harmonic it can point directly to Rx amplitude mismatch due to routing modification. Then engineers can further optimize the coils routing. The SHAP results can be used by engineers to decide which factors require tight control (e.g., Y and tilt in this study) and which can be relaxed. Thus, we can provide installation suggestions to customers, focusing alignment effort on the most influential misalignment directions instead of uniformly tightening all dimensions.

4. Conclusions

This paper presented and validated a compact two-layer PCB routing strategy for an inductive MPS under realistic installation tolerances. A comprehensive DOE covering 625 combinations of X/Y offsets, tilt, and airgap (±0.5 mm in X/Y, ±0.5° tilt, 1.9–3.1 mm airgap) showed that all test cases remained within ±1 electrical degree, demonstrating that the 2L layout can satisfy typical automotive accuracy requirements. The Fourier series on the circle analysis shows that the DC offset and magnitudes mismatch of the 3 Rx signals are the dominant error contributors. An XGBoost regression model trained on test data achieved high fidelity with R^2=0.9951, RMSE = 0.3105, MAE = 0.2192. SHAP analysis revealed misalignment effects. Tilt and Y-offset are the dominant contributors to accuracy degradation. X-offset and airgap exhibits a smaller influence and weak interactions. These results show that the proposed 2L routing achieves robust angle accuracy across realistic misalignment ranges and that the workflow offers a general, quantitative approach for analyzing inductive MPS layouts and installation tolerances in future designs.

Future work will focus on identifying quantitative dimensional thresholds for both 2-layer and 4-layer PCB configurations. Establishing these boundaries will enable engineers to make informed cost–performance trade-offs and to select the most appropriate layer configuration for a given application, thereby guiding the deployment of next-generation, low-cost inductive MPSs with predictable installation robustness.

Author Contributions: Conceptualization, methodology, software, validation, formal analysis, investigation, data curation, writing—original draft preparation, writing—review and editing, and visualization, Q.L. and D.S.; Resource, Experimental setup, Data acquisition system, D.M.; PCB layout implementation, D.T. All authors have read and agreed to the published version of the manuscript.

Funding: This research received no external funding.

Data Availability Statement: The datasets generated during the current study are not publicly available due to company confidentiality. Data sharing is not applicable to this article.

Conflicts of Interest: The authors declare no conflicts of interest.

References

1. U.S. DRIVE Partnership, *Electric Technical Team Roadmap*, U.S. Department of Energy, 2024. https://www.energy.gov/sites/default/files/2024-06/EDTT_Roadmap_2023_JOG_Consensus_compliant.pdf
2. Datlinger, C.; Hirz, M. Benchmark of Rotor Position Sensor Technologies for Application in Automotive Electric Drive Trains. *Electronics* **2020**, *9*, 1063. https://doi.org/10.3390/electronics9071063
3. Datlinger C, Hirz M. Evaluation of signal processing effects on rotor position sensor systems for electric traction motors. In Conference EAEC 2017, Madrid, Spain, 03-05, Oct. 2017.

4. Li, Y.; Wu, H.; Xu, X.; Sun, X.; Zhao, J. Rotor Position Estimation Approaches for Sensorless Control of Permanent Magnet Traction Motor in Electric Vehicles: A Review. *World Electr. Veh. J.* **2021**, *12*, 9. https://doi.org/10.3390/wevj12010009
5. De Klerk, M. L. and Saha, A. K. A Comprehensive Review of Advanced Traction Motor Control Techniques Suitable for Electric Vehicle Applications, in *IEEE Access*, vol. 9, pp. 125080-125108, 2021, doi: 10.1109/ACCESS.2021.3110736.
6. Murray, A., Hare, B. and Hirao, A. Resolver position sensing system with integrated fault detection for automotive applications, *SENSORS, 2002 IEEE*, Orlando, FL, USA, 2002, pp. 864-869 vol.2, doi: 10.1109/ICSENS.2002.1037221.
7. Leibovich, G. and Senanian, S. Development of Variable Reluctance Resolver for Position Feedback, Proceedings of the 41st Aerospace Mechanisms Symposium, Jet Propulsion Laboratory, May 16-18, 2012
8. Hobein, D., Dorißen, T., and Dürkopp, K., Progress in Automotive Position Sensors and Introduction of the Hella Inductive Position Sensor, SAE Technical Paper 2004-01-1115, 2004, https://doi.org/10.4271/2004-01-1115.
9. Lugani, L., Akermi, Y., Laval, P. and Duisters, A. *High Speed Inductive Position Sensor for E-Machines*. Melexis, white paper, 2021.
10. S. Kuntz, G. Gerlach, S. Fella. Inductive Position Sensors based on Coupling of Coils on Printed Circuit Boards for Demanding Automotive Applications. arXiv:2503.14627v1.
11. Shao, L., Automotive Inductive Position Sensor. Doctor of Philosophy degree in Mechanical and Materials Engineering, Western University, London, Ontario, Canada, 5th May 2017. Electronic Thesis and Dissertation Repository. https://ir.lib.uwo.ca/etd/4569 (accessed on 5 May 2017).
12. Kuntz, S.; Gerber, D.; Gerlach, G.; Fella, S. Design and Analysis of Receiver Coils with Multiple In-Series Windings for Inductive Eddy Current Angle Position Sensors Based on Coupling of Coils on Printed Circuit Boards. *Sensors* **2024**, *24*, 4880. https://doi.org/10.3390/s24154880
13. Chen, T.; Guestrin, C. *XGBoost: A Scalable Tree Boosting System*. In *Proceedings of the 22nd ACM SIGKDD International Conference on Knowledge Discovery and Data Mining*, San Francisco, CA, USA, 2016.
14. Lundberg, S.M.; Lee, S.I. A Unified Approach to Interpreting Model Predictions. Advances in Neural Information Processing Systems 2017, 30, 4765–4774.
15. Lundberg, S.M.; Erion, G.G.; Lee, S.I. Consistent Individualized Feature Attribution for Tree Ensembles. arXiv preprint arXiv:1802.03888, 2018
16. Nuyts, L., Davis, J. The When and How of Target Variable Transformations. In: Krempl, G., Puolamäki, K., Miliou, I. (eds) Advances in Intelligent Data Analysis XXIII. IDA 2025. Lecture Notes in Computer Science, vol 15669. Springer, Cham. https://doi.org/10.1007/978-3-031-91398-3_9
17. Friedman, J.H. *Greedy Function Approximation: A Gradient Boosting Machine. Annals of Statistics*, 2001, 29(5), 1189–1232.
18. Singh, A. 0K., Raja, R., Sebastian, T. and Gebregergis, A. Effect of Position Measurement Delay on the Performance of PMSM Drive, *2018 IEEE Energy Conversion Congress and Exposition (ECCE)*, Portland, OR, USA, 2018, pp. 4622-4627, doi: 10.1109/ECCE.2018.8558059.
19. Pramod, P. Position Sensing Errors in Synchronous Motor Drives. *arXiv* **2023**, arXiv:2310.00977
20. SHAP. An Introduction to Explainable AI with Shapley Values. Read the Docs. Available online: https://shap.readthedocs.io/en/latest/example_notebooks/overviews/An%20introduction%20to%20explainable%20AI%20with%20Shapley%20values.html (accessed on 7 November 2025).